Learning acoustic responses from experiments: A multiscale-informed transfer learning approach

Van Hai Trinh, Johann Guilleminot, Camille Perrot, et al.

Citation: The Journal of the Acoustical Society of America **151**, 2587 (2022); doi: 10.1121/10.0010187
View online: https://doi.org/10.1121/10.0010187
View Table of Contents: https://asa.scitation.org/toc/jas/151/4
Published by the Acoustical Society of America

JASA ARTICLE

Learning acoustic responses from experiments: A multiscale-informed transfer learning approach

Van Hai Trinh,[1] Johann Guilleminot,[2] Camille Perrot,[3,a)] and Viet Dung Vu[4]

[1]*Faculty of Vehicle and Energy Engineering, Le Quy Don Technical University, 236 Hoang Quoc Viet, Ha Noi, Vietnam*

[2]*Department of Civil and Environmental Engineering, Duke University, Durham, North Carolina 27708, USA*

[3]*Univ Gustave Eiffel, Univ Paris Est Creteil, CNRS, UMR 8208, MSME, F-77454 Marne-la-Vallée, France*

[4]*Department of Mechanical Engineering, Université de Sherbrooke, Sherbrooke, Quebec, J1K 2R1, Canada*

ABSTRACT:

A methodology to learn acoustical responses based on limited experimental datasets is presented. From a methodological standpoint, the approach involves a multiscale-informed encoder used to cast the learning task in a finite-dimensional setting. A neural network model mapping parameters of interest to the latent variables is then constructed and calibrated using transfer learning and knowledge gained from the multiscale surrogate. The relevance of the approach is assessed by considering the prediction of the sound absorption coefficient for randomly-packed rigid spherical beads of equal diameter. A two-microphone method is used in this context to measure the absorption coefficient on a set of configurations with various monodisperse particle diameters and sample thicknesses, and a hybrid numerical approach relying on the Johnson-Champoux-Allard-Pride-Lafarge model is deployed as the multiscale-based predictor. It is shown that the strategy allows for the relationship between the micro-/structural parameters and the experimental acoustic response to be well approximated, even if a small physical dataset (comprised of ten samples) is used for training. The methodology, therefore, enables the identification and validation of acoustical models under constraints related to data limitation and parametric dependence. It also paves the way for an efficient exploration of the parameter space for acoustical materials design. © *2022 Acoustical Society of America*.

https://doi.org/10.1121/10.0010187

(Received 20 October 2021; revised 15 March 2022; accepted 25 March 2022; published online 13 April 2022)

[Editor: Kirill V. Horoshenkov] Pages: 2587–2601

I. INTRODUCTION

The analysis of the relationship between microstructural parameters and ultimate acoustic performance is a fundamental question that has attracted much attention over the past two decades. Various frameworks and variations thereof were proposed to understand the underlying physical mechanisms and to predict acoustical properties for different types of materials, including the use of purely phenomenological,[1–4] semi-phenomenological,[5–10] semi-analytical,[11–13] and multiscale models;[14–17] see Refs. 18 and 19 for a review. Most of these approaches are found to produce reasonably accurate estimations within their respective range of applicability, even if some discrepancies between model predictions and experimental responses are sometimes observed for certain classes of materials, such as nonlinear metamaterials.[20,21] While a large body of the literature has focused on bottom-up approaches, predicting acoustic performance based on microstructural descriptors, the relationship may also be investigated as a top-down approach, solving an inverse problem to infer microstructural parameters based on coarse-scale measurements. In this context, the Bayesian approach to parameter identification was applied in Ref. 22 to calibrate the geometrical, transport, and elastic properties characterizing the elasto-acoustic behavior of poro-elastic materials. More recently, so-called data-driven approaches have emerged with the aim of learning forward or inverse models based on datasets. The use of neural network models, in particular, was proposed as a means to represent potentially highly nonlinear maps in very high-dimensional settings (see Ref. 23 for a review in acoustics, as well as Ref. 24 for an application involving convolutional neural networks). Physics-informed formulations involving residuals from parametric partial differential equations were proposed to bridge the gap between established physical theories and approaches solely relying on data science (see the seminal work,[25] for instance). Deep learning techniques are often meant to be operated in the big data limit, that is, for very large datasets. This assumption may be deemed inadequate in scientific machine learning where practical applications typically involve limited physical experiments.

The goal of this work is to propose a methodology that circumvents data limitations for learning experimental acoustic responses parameterized by microstructural and sample properties. Specifically, we address the calibration of a neural network model using a small dataset—typically comprised of a few experimental results—by leveraging information gained through a standard multiscale analysis. It is important to emphasize at this point that the aim of this study is not to assess the performance or to promote the use

a)Electronic mail: camille.perrot@univ-eiffel.fr

of one class of methods against the other (that is, physics-based versus data-driven models), for a specific regression problem. We rather focus on the development of a methodology that combines these two ingredients in a synergistic manner, to address a question that remains hard to tackle using any of these methods independently. Borrowing ingredients from multi-fidelity modeling[26] and operator learning,[27] we first introduce an appropriate simulation-based representation that encodes the experimental response in the frequency domain. Here, we consider the prediction of the sound absorption coefficient as a prototypical application. We then develop a neural network model between input parameters of interest and the reduced variables defined by the encoder. We finally use a transfer learning approach to compensate for data scarcity at the training stage.

This paper is organized as follows. The overall methodology and technical ingredients are presented in Sec. II. We discuss, in particular, the encoding-decoding strategy and learning aspects. We then deploy and analyze the performance of the approach in Sec. III. We specifically consider the case of sound absorption measurements and introduce both the experimental setting and the associated computational surrogate model. We show that the framework enables the prediction of experimental results with a fairly good accuracy (quantified in the L^2 sense), even with limited data. Concluding remarks are finally provided in Sec. IV.

II. METHODOLOGY

A. Overview of the approach

We seek a surrogate model mapping some input (material or microstructural) parameters to the sound absorption coefficient over some angular frequency range, denoted by $\mathbb{W}$. Let $\boldsymbol{\mu} \mapsto \{\alpha(\omega;\boldsymbol{\mu}), \omega \in \mathbb{W}\}$ be the forward map of interest, where $\boldsymbol{\mu}$ is the vector of input parameters, α is the sound absorption coefficient, and $\mathbb{W}$ is assumed to be the Cartesian product of closed intervals. Our goal is to construct a methodology that allows one to learn this forward map, using results from a *limited* set of physical experiments.

Owing to a probabilistic interpretation of $\boldsymbol{\mu}$, which is assumed to be defined on some probability space $(\Theta, \mathcal{F}, P)$ (where Θ denotes the sample space, $\mathcal{F}$ is a σ-field, and P is a probability measure), and assuming that $\alpha \in L^2(\Theta, L^2(\mathbb{W}))$ (notice that α is of second-order as it is bounded almost surely), the process $\{\alpha(\omega), \omega \in \mathbb{W}\}$ can be represented through its Karhunen-Loève (KL) expansion,[28]

$$\alpha(\omega) = \underline{\alpha}(\omega) + \sum_{i=1}^{+\infty} \sqrt{\lambda_i}\eta_i\varphi_i(\omega), \tag{1}$$

where $\omega \mapsto \underline{\alpha}(\omega)$ is the mean function of the sound absorption coefficient (that is, $\underline{\alpha}(\omega) = \mathbb{E}\{\alpha(\omega)\}$ for all $\omega \in \mathbb{W}$), the pairs $\{(\lambda_i, \varphi_i)\}_{i\geq 1}$ are the eigenvalues and eigenfunctions of the covariance operator satisfying the integral equation,

$$\int_{\mathbb{W}} C(\omega,\omega')\varphi_i(\omega')\,d\omega' = \lambda_i\varphi_i(\omega), \tag{2}$$

where $(\omega,\omega') \mapsto C(\omega,\omega')$ is the covariance function of $\{\alpha(\omega), \omega \in \mathbb{W}\}$, and the reduced variables $\{\eta_i\}_{i\geq 1}$ are defined as

$$\eta_i = \frac{1}{\sqrt{\lambda_i}}\langle \alpha - \underline{\alpha}, \varphi_i\rangle, \tag{3}$$

with $\langle\cdot,\cdot\rangle$ the inner product between functions,

$$\langle f, g\rangle = \int_{\mathbb{W}} f(\omega)g(\omega)\,d\omega. \tag{4}$$

The variables $\{\eta_i\}_{i\geq 1}$ are centered, have unit variance, and are pairwise uncorrelated. Notice that we did not adapt the notation to reflect the stochastic interpretation in the above equations for simplicity. The truncated expansion reads as

$$\alpha_\nu(\omega) = \underline{\alpha}(\omega) + \sum_{i=1}^{\nu} \sqrt{\lambda_i}\eta_i\varphi_i(\omega), \tag{5}$$

where the order ν is determined through a convergence analysis and α_ν converges to α in the mean square sense as $\nu \to +\infty$.

One natural path to learn the mapping $\boldsymbol{\mu} \mapsto \{\alpha(\omega;\boldsymbol{\mu}), \omega \in \mathbb{W}\}$ then consists (i) of estimating the mean $\underline{\alpha}$ and the set of eigenpairs $\{(\lambda_i, \varphi_i)\}_i^\nu$ from a given dataset, and (ii) learning the mapping $\boldsymbol{\mu} \mapsto \boldsymbol{\eta}(\boldsymbol{\mu})$ between the input parameters and the latent reduced variables with $\boldsymbol{\eta}(\boldsymbol{\mu}) = (\eta_1(\boldsymbol{\mu}), \ldots, \eta_\nu(\boldsymbol{\mu}))^T$. There are two main benefits of proceeding this way. First, the learning task is now cast in a finite dimensional space (that is, in $\mathbb{R}^\nu$), as proposed in Ref. 27, e.g., for the learning between Hilbert spaces for instance. Second, the use of a basis in the frequency domain renders the approximation more robust to noise in the data. Since we are interested in learning from experiments, it is convenient to introduce the following truncated decomposition, related to observations,

$$\alpha_\nu^{\text{exp}}(\omega) = \underline{\alpha}^{\text{exp}}(\omega) + \sum_{i=1}^{\nu} \sqrt{\lambda_i^{\text{exp}}}\eta_i^{\text{exp}}\varphi_i^{\text{exp}}(\omega). \tag{6}$$

In Eq. (6), the superscript "exp" indicates that all quantities are computed based on the experimental results, using statistical estimators. In a standard setting where few samples are available (meaning that the physical experiments are conducted for a few choices of input parameters, typically less than 10), the covariance operator estimated from the data is, however, often found to be non-positive, hence making the above formulation ill-posed. To circumvent that limitation and properly set up the learning task, we propose the following two-step "regularization" approach.

(i) First, a numerical multiscale-informed surrogate model for the experiments is introduced. We denote by $\{\alpha^{\text{sim}}(\omega), \omega \in \mathbb{W}\}$ the sound absorption coefficient thus obtained, and we consider the truncated KL expansion,

https://doi.org/10.1121/10.0010187

$$\alpha_\nu^{\text{sim}}(\omega) = \underline{\alpha}^{\text{sim}}(\omega) + \sum_{i=1}^{\nu} \sqrt{\lambda_i^{\text{sim}}}\,\eta_i^{\text{sim}}\,\varphi_i^{\text{sim}}(\omega), \tag{7}$$

with notation analogous to Eq. (6).

(ii) Second, the (centered) experimental data are projected onto the computational basis,

$$\alpha_\nu^{\text{exp}}(\omega) = \underline{\alpha}^{\text{exp}}(\omega) + \sum_{i=1}^{\nu} \sqrt{\lambda_i^{\text{sim}}}\,\hat{\eta}_i^{\text{exp}}\,\varphi_i^{\text{sim}}(\omega), \tag{8}$$

where the same truncation order is assumed, without loss of generality, and

$$\hat{\eta}_i^{\text{exp}} := \frac{1}{\sqrt{\lambda_i^{\text{sim}}}} \langle \alpha^{\text{exp}} - \underline{\alpha}^{\text{exp}}, \varphi_i^{\text{sim}} \rangle. \tag{9}$$

The hat symbol in Eq. (9) is used to emphasize that the reduced coordinates are different from those in Eq. (6) (see the remark below). The mapping $\boldsymbol{\mu} \mapsto \hat{\boldsymbol{\eta}}^{\text{exp}}(\boldsymbol{\mu})$ is subsequently approximated by using transfer learning with neural network models, using prior knowledge gained by developing a surrogate model for the mapping $\boldsymbol{\mu} \mapsto \boldsymbol{\eta}^{\text{sim}}(\boldsymbol{\mu})$.

It should be noticed that the above approach can be interpreted, to some extent, in a multi-fidelity setting where α^{exp} represents information that is costly to collect, while the numerical approximation α^{sim} remains cheaper to synthesize in general. A study about transfer learning in this context can be found in Ref. 26, for instance. Moreover, the use of a KL expansion rises theoretical issues pertaining to approximation capabilities for the neural networks, due to the non-compactness of the latent spaces. This fundamental aspect is beyond the scope of this work, and we refer to Ref. 27 for a discussion. The ingredients of the above framework are presented in the following sections.

Remark: It is important to note that Eq. (8) does not correspond to the KL expansion of the process $\{\alpha^{\text{exp}}(\omega), \omega \in \mathbb{W}\}$. In particular, the right-hand side is not optimal in the L^2 sense, and the reduced variables $\{\hat{\eta}_i\}_{i=1}^{\nu}$, while centered, are not pairwise uncorrelated. The representation is, however, licit since $\{\varphi_i^{\text{sim}}\}_{i\geq 1}$ constitutes an orthonormal basis of $L^2(\mathbb{W})$ (which follows from the properties of the covariance operator).

B. Neural networks as surrogate models

In this section, we recall the necessary background on (feed-forward) neural networks and transfer learning. Providing general reviews on these very active research topics is beyond the scope of this work, and we refer interested readers to Ref. 29 and Refs. 30 and 31 for discussions, for instance.

1. Background

A neural network surrogate aims to map some input vector-valued parameter $\boldsymbol{x} \in \mathbb{R}^{\mathcal{I}}$ to some output (vector-valued) parameter $\boldsymbol{y} \in \mathbb{R}^{\mathcal{O}}$, using a composite transformation that (i) involves input and output layers, as well as so-called hidden layers that each contains a set of neurons; and (ii) is learned on a training data set $\mathcal{D} = \{\boldsymbol{x}^{(i)}, \boldsymbol{y}^{(i)}\}_{i=1}^{N_D}$ with N_D data points. Following standard notation, we denote by N_H the total number of hidden layers and let n_ℓ be the number of neurons in the ℓ th layer. In this work, we consider a feed-forward neural network in which the output of the jth neuron in a given layer is produced by transmitting a weighted sum of input signals (from the preceding layer), plus a bias, to an activation (or transfer) function ϕ_a:

$$z_j^{(\ell)} = \phi_a\left(\sum_{i=1}^{n_{\ell-1}} W_{ij}^{(\ell)} z_i^{(\ell-1)} + \theta_j^{(\ell)}\right), \quad 1 \leq j \leq n_\ell, \quad 1 \leq \ell \leq N_H, \tag{10}$$

with $z_i^{(0)} = x_i$, $1 \leq i \leq \mathcal{I}$. The components of the output layer are defined as

$$y_j = \sum_{i=1}^{n_{N_H}} W_{ij}^{(0)} z_i^{(N_H)} + \theta_j^{(0)}, \quad 1 \leq j \leq \mathcal{O}. \tag{11}$$

In the above equations, $W_{ij}^{(\ell)}$ denotes the weight for the connection between the ith neuron in layer $(\ell - 1)$ and the jth neuron in layer ℓ, and $\theta_j^{(\ell)}$ is the bias corresponding to the jth neuron in layer ℓ. The neural network is therefore parameterized by the sets $\{\boldsymbol{W}^{(\ell)}\}_{\ell=0}^{N_H}$ and $\{\theta^{(\ell)}\}_{\ell=0}^{N_H}$ of weight matrices and bias vectors, where $\boldsymbol{W}^{(0)}$ and $\theta^{(0)}$ are associated with the output layer by convention, and

$$\boldsymbol{W}^{(\ell)} = \left[W_{ij}^{(\ell)}\right] \in \mathbb{M}_{n^{(\ell-1)} \times n^{(\ell)}}(\mathbb{R}),$$
$$\theta^{(\ell)} = \left[\theta_j^{(\ell)}\right] \in \mathbb{M}_{1 \times n^{(\ell)}}(\mathbb{R}). \tag{12}$$

There exist many choices for the activation function, including the Rectified Linear Unit (ReLU), sigmoid, and hyperbolic tangent functions for instance; see Ref. 29. In this paper, we use the sigmoid function $\phi_a(v) = 1/[1 + \exp(-v)]$ for all hidden layers, and the architecture of the neural networks was determined through parametric analyses on validation errors.

An important step while using neural networks pertains to training, that is, to the calibration of the weight matrices $\{\boldsymbol{W}^{(\ell)}\}_{\ell=0}^{N_H}$ and bias vectors $\{\theta^{(\ell)}\}_{\ell=0}^{N_H}$. This is commonly achieved by minimizing a loss function, potentially supplemented with a regularization term, and many techniques were proposed in the literature.[29] We use a standard supervised approach based on the minimization of the mean squared error,

$$\ell(\{\boldsymbol{W}^{(\ell)}, \theta^{(\ell)}\}_{\ell=0}^{N_H}) = \frac{1}{N_D} \sum_{i=1}^{N_D} \left\| \hat{\boldsymbol{y}}(\boldsymbol{x}^{(i)}; \{\boldsymbol{W}^{(\ell)}, \theta^{(\ell)}\}_{\ell=0}^{N_H}) - \boldsymbol{y}^{(i)} \right\|^2, \tag{13}$$

where $\hat{\boldsymbol{y}}(\boldsymbol{x}^{(i)}; \{\boldsymbol{W}^{(\ell)}, \theta^{(\ell)}\}_{\ell=0}^{N_H})$ denotes the prediction of the neural network parameterized by $\{\boldsymbol{W}^{(\ell)}, \theta^{(\ell)}\}_{\ell=0}^{N_H}$ at the data point $\boldsymbol{x}^{(i)}$.

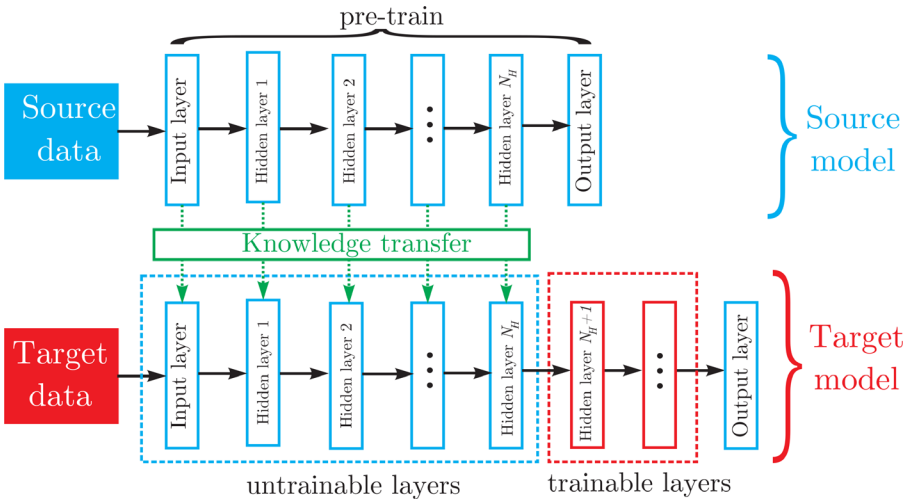

FIG. 1. (Color online) Principles of transfer learning for regression problems. A neural network is first pretrained using data from a similar problem, associated with a source model (top row). Knowledge gained through this training is subsequently transferred to train an adapted neural network surrogate for the target model (bottom row). Here, this adaptation corresponds to an extension of the pretrained model through the addition of hidden layers.

In this work, various algorithms for network training were tested through parametric analyses, including the Levenberg-Marquardt and stochastic gradient descent techniques. Most algorithms were found to provide similar results, and the results provided in Sec. III C were obtained with the Levenberg-Marquardt optimizer.

2. Transfer learning

In the context of inductive learning for regression problems (see Refs. 30 and 31 for reviews with applications to classification and regression), transfer learning proceeds by adapting an existing neural network that has been pretrained on data generated by a similar problem. This principle is schematically depicted in Fig. 1, using the terminology introduced in the aforementioned references.

The adaptation can be performed, for instance, by preserving the structure of the pretrained network and by updating its parameters in either all or a few layers, or by adding hidden layers to approximate the mapping $\boldsymbol{\eta}^{\mathrm{sim}} \mapsto \hat{\boldsymbol{\eta}}^{\mathrm{exp}}(\boldsymbol{\eta}^{\mathrm{sim}})$. In this work, we use the second approach given the analogy between Eqs. (7) and (8), where α^{sim} is assumed to be a reasonable proxy for α^{exp}.

III. APPLICATION TO EXPERIMENTAL MEASUREMENTS FOR THE SOUND ABSORPTION COEFFICIENT

In this section, we deploy the methodology presented in Sec. II A. The experimental analysis is first presented in Sec. III A. The multiscale surrogate used for computing the projection basis and transfer learning is then discussed in Sec. III B. The learning strategy is finally exemplified in Sec. III C.

Owing to a slight abuse of notation, we consider the sound absorption coefficient to be expressed as a function of the angular frequency ω or the frequency f (with $\omega = 2\pi f$), and denote by α the aforementioned coefficient regardless of the associated variable.

A. Description of the physical experiments

In order to illustrate the approach, we consider the characterization of the sound absorption coefficient for randomly-packed rigid spherical beads. To that end, ten samples with various combinations of monodisperse bead diameter and sample thickness were processed; see Table I and Fig. 2(a). Bead diameters were provided by the manufacturer and are sufficiently accurate for long wavelength acoustical purposes.

A two-microphone method was used to estimate the sound absorption coefficient of the porous media at normal incidence, by measuring the pressure transfer function $H_{12} = p_1/p_2$, in which p_1 and p_2 are the pressures determined at the two microphones; see Figs. 2(b) and 2(c). A steel net is used to control the sample thickness; see Fig. 2(c). It is worth noticing that manual measurements of the sample packing fraction can be expected to be less precise for large bead diameters. The sound absorption coefficient is then experimentally estimated as

$$\alpha^{\mathrm{exp}} = 1 - \left| \frac{\exp(jk_a d_{12}) - H_{12}}{H_{12} - \exp(-jk_a d_{12})} \exp(2jk_a d_{2s}) \right|^2, \quad (14)$$

in which k_a represents the wavenumber in the ambient fluid, d_{12} is the distance between microphones 1 and 2, and d_{2s} is the distance between microphone 2 and the front surface of the porous sample.[32] Measurements were conducted with an impedance tube of length 1 m and inner diameter 40 mm [see Fig. 2(b)], in the frequency range [100, 4500] Hz with a sampling step of 4 Hz. The experimental results are reported in Fig. 3.

TABLE I. Definition of the experimental samples.

	Sample #									
Parameter	R1	R2	R3	R4	R5	R6	R7	R8	R9	R10
Diameter, d [mm]	3	4	5	6	7	3	4	5	6	7
Thickness, L [mm]	23.5	23.5	23.5	23.5	23.5	47	47	47	47	47

https://doi.org/10.1121/10.0010187

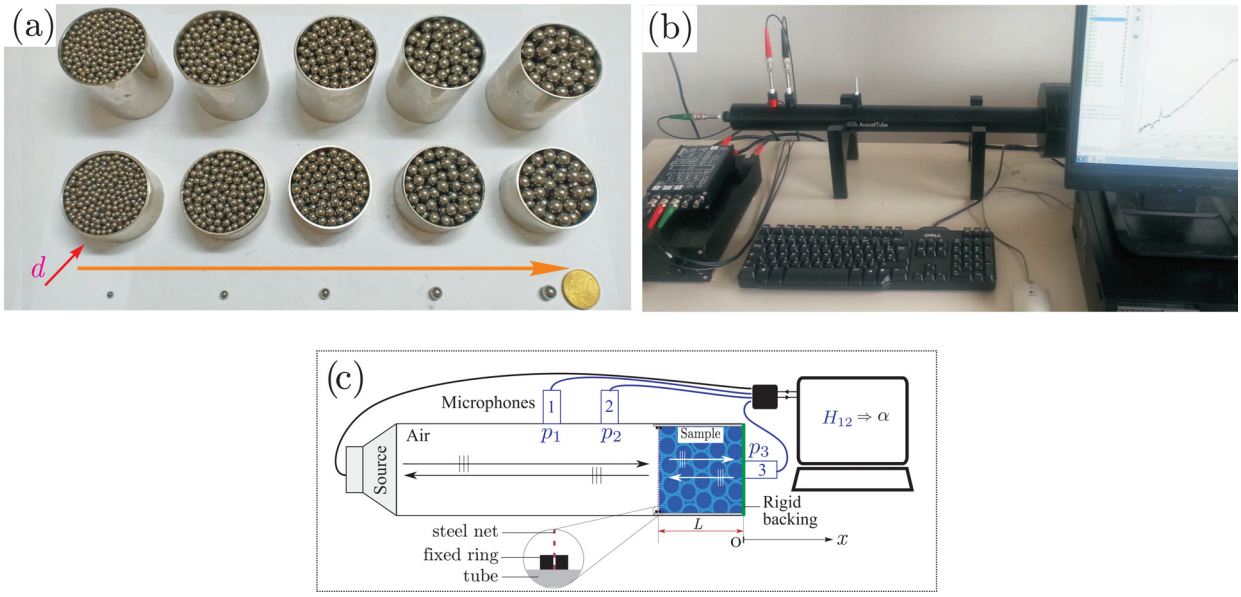

FIG. 2. (Color online) (a) Samples of randomly-packed rigid spherical beads. The top row corresponds to sphere layers with a thickness of 47 mm, while the bottom row shows 23.5 mm-thick layers. (b), (c) Acoustical measurement setup and impedance tube configuration. Note that the specimen is backed by a rigid wall.

The normal incidence sound absorbing behavior of monodisperse spherical particles has been discussed elsewhere; see Ref. 33, Sec. VIII (and Refs. 34 and 35) for instance. Indeed, it was shown that accurate predictions of the first sound absorption peak can be obtained in terms of frequency and magnitude from the geometrical properties of the material (d, L). The first normal incidence sound absorption peak corresponds to the quarter wavelength resonant absorption of the material and is governed by its intrinsic damped wavelength λ_{eq} (and not directly by the wavelength in the air). The successive maxima appear at the quarter wavelength, where $L/\Re e(\lambda_{eq}) = n/4$, with n being successive odd integers. The thickness-to-particle-diameter ratio L/d controls the magnitude of the first sound absorption peak and the optimal value of the thickness-to-particle-diameter ratio N_{opt} allowing 100% absorption at a given particle diameter was found to be a linear function of the particle diameter [see Fig. 12 and Eq. (35) of Ref. 33]. Our experimental results are consistent with the systematic analysis proposed in Ref. 33, in which the optimal particle diameter is given, for a given thickness L, as $d_1(L) = \sqrt{L/\delta_1}$ (with $\delta_1 = 12\,494\ \mathrm{m}^{-1}$; see Ref. 33). Note that symbols d_1 and δ_1 are used hereinafter for consistency with Ref. 33. For the two considered layer thicknesses, optimal particle diameters are estimated as $d_1(L = 23.5\,\mathrm{mm}) = 1.4\,\mathrm{mm}$ and $d_1(L = 47\,\mathrm{mm}) = 1.9\,\mathrm{mm}$. This explains why the sound absorption magnitude of sample R6 reaches a maximum value above 0.9, whereas the first peak magnitude of sample R1 is much lower than this critical value—even if the two samples involve the same particle diameter, $d = 2\,\mathrm{mm}$. The information described above constitutes the dataset for the experimental response $\boldsymbol{\mu} \mapsto \{\alpha^{\exp}(\omega; \boldsymbol{\mu}), \omega \in \mathbb{W}\}$, with $\boldsymbol{\mu} = (d, L)^T$.

B. Multiscale surrogate

We now introduce the computational surrogate for the experiments described in Sec. III A. Additional results pertaining to code verification and model accuracy are reported in the Appendix A.

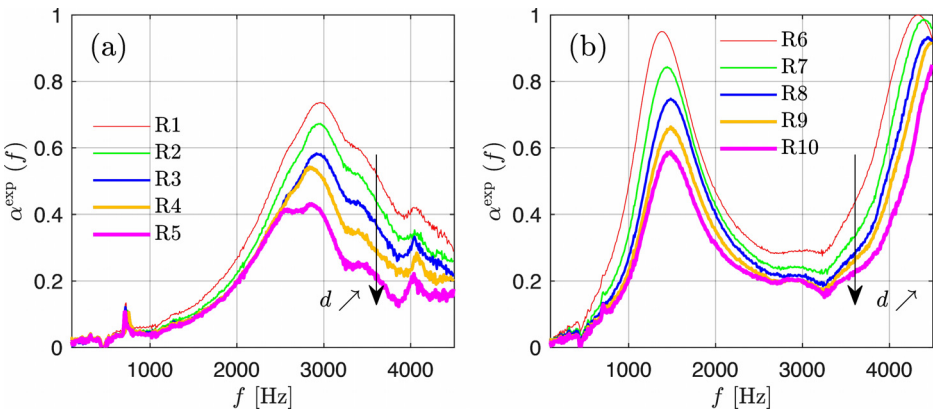

FIG. 3. (Color online) Experimentally-measured sound absorption coefficients estimated for the samples described in Table I.

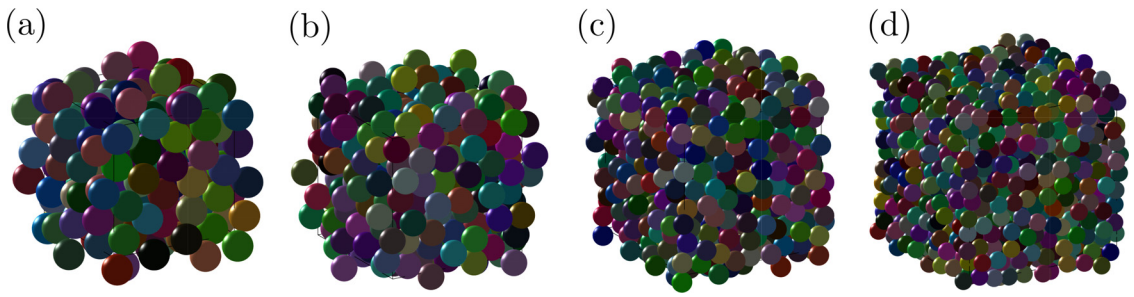

FIG. 4. (Color online) Realizations of the random close packing obtained for $N = 128$, $N = 256$, 512, and $N = 1024$ (from left to right), for a solid volume fraction set to 0.6.

1. Microstructural sampling

The first step consists in sampling a random close packing of mono-sized rigid spheres (for a given value of $\boldsymbol{\mu}$). To that aim, we rely on the algorithm proposed in Refs. 36 and 37 where spheres are randomly distributed within the domain at initialization and moved, in an iterative manner, to avoid overlaps and reach a target packing fraction. In order to enforce a periodic structure at the boundaries of the simulation domain, each sphere intersecting with p faces at the boundary ($1 \leq p \leq 3$) is duplicated p times, and the center of each replicate is translated towards the face opposing the intersecting boundary by a factor equal to the size of the domain.[38] Four sphere ensembles with a target solid volume fraction of 0.6 are shown in Fig. 4, for the sake of illustration. The radial distribution function g for several packing configurations is shown in Fig. 5. The generation of a microstructure with $N = 128$, 512, and 1024 spheres took about 35, 255, and 1523 s, respectively, on a laptop equipped with an Intel(R) Core(TM) i7-4500U (Intel, China) cadenced at 2.40 GHz.

2. Determination of the transport properties

The second step involves the calculation of transport properties using the periodic solid skeleton defined in Sec. III B 1.

Let Ω be the reconstructed Representative Volume Element (RVE) under consideration with boundary $\partial\Omega$, and let its solid phase, fluid, and fluid-solid interface be denoted by Ω_s, Ω_f, and $\partial\Omega_f$, respectively. The porosity (or fluid volume fraction) ϕ and the thermal characteristic length (or generalized hydraulic radius) Λ' are directly obtained as

$$\phi = \frac{\int_{\Omega_f} dV}{\int_{\Omega} dV}, \quad \Lambda' = 2\frac{\int_{\Omega_f} dV}{\int_{\partial\Omega_f} dS}. \tag{15}$$

The macroscopic transport properties can be computed from the numerical solutions of a series of canonical boundary value problems, namely, (i) a viscous flow problem, for the static viscous permeability k_0 and static viscous tortuosity α_0;[5,7,8,39] (ii) an inertial flow problem, for the viscous characteristic length Λ and the high frequency tortuosity α_∞;[5,40,41] and (iii) a steady-state heat conduction problem, enabling for the static thermal permeability k_0' and the static thermal tortuosity α_0' to be computed.[7,9,42] These boundary value problems are recalled below for the sake of self-containedness; interested readers are referred to the literature[19,39,43,44] for the first-principles calculations of these transport properties.

a. Viscous flow. This problem corresponds to the low frequency limit (that is, when $\omega \to 0$) where viscous effects dominate, hence creating a steady-state flow in the porous media. The flow, associated with an incompressible Newtonian fluid at very low Reynolds numbers, is described by the scaled Stokes problem,[39]

$$-\nabla^2 \mathbf{k}_0^\star + \nabla \pi_0^\star = \mathbf{e}, \quad \nabla \cdot \mathbf{k}_0^\star = 0, \tag{16}$$

in Ω_f, with $\mathbf{k}_0^\star = \mathbf{0}$ on $\partial\Omega_f$ and where the scaled velocity $\mathbf{k}_0^\star$ and pressure $\pi_0^\star$ of the fluid are Ω-periodic. Here, $\mathbf{e}$ is a unitary vector corresponding to the imposed macroscopic pressure

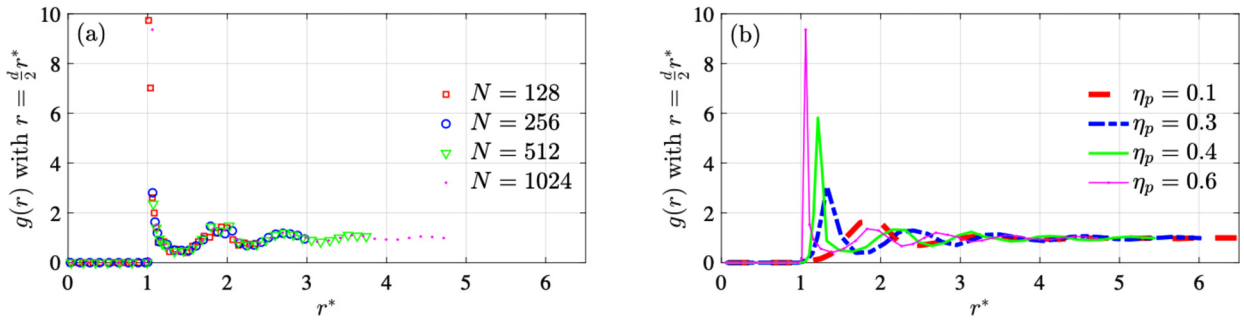

FIG. 5. (Color online) Graph of the function $g(r) \to r^*(= 2r/d)$ for: (a) various numbers N with a value of solid volume fraction $\eta_p = 0.60$, and (b) several packing fractions η_p with $N = 1024$.

https://doi.org/10.1121/10.0010187

gradient that drives the flow in a preferential direction. The symbol ∇ denotes the nabla differential operator, while the dot symbol "$\cdot$" denotes the classical inner product in $\mathbb{R}^3$. The separation of scales (and thereby, macroscopic isotropy) is assumed for the considered microstructure.[45] The static viscous permeability k_0 and the static viscous tortuosity α_0 are then calculated as[43,44]

$$k_0 = \phi \langle \mathbf{k}_0^\star \cdot \mathbf{e} \rangle , \quad \alpha_0 = \frac{\langle \mathbf{k}_0^\star \cdot \mathbf{k}_0^\star \rangle}{\langle \mathbf{k}_0^\star \rangle \cdot \langle \mathbf{k}_0^\star \rangle}, \tag{17}$$

where $\langle \bullet \rangle$ indicates spatial averaging over the fluid domain. Notice that the aforementioned scalar transport parameters are sufficient to describe the (isotropic) static viscous permeability and tortuosity tensors.

b. Inertial flow. This problem is associated with the high-frequency regime, $\omega \to +\infty$. In this case, inertial forces dominate over viscous ones and, consequently, the saturating fluid tends to behave as a nearly perfect fluid (without viscosity except in the vicinity of the boundary layer). The inertial flow of the perfect incompressible fluid then formally behaves according to an electric conduction phenomenon (where the porous material is composed of a non-conducting solid matrix and a conducting fluid).[5,40,41] Quantities of interest in the inertial flow problem can be thus obtained by solving the following set of potential equations:

$$\mathbf{E} = -\nabla \varphi + \mathbf{e} , \quad \nabla \cdot \mathbf{E} = 0, \tag{18}$$

in Ω_f, subjected to $\mathbf{E} \cdot \mathbf{n} = 0$ on $\partial\Omega_f$ and φ is Ω-periodic. In the above equations, $\mathbf{e}$ is a given macroscopic electric field, $\mathbf{E}$ is the local solution to the boundary value problem having $-\nabla\varphi$ as a fluctuating part, and $\mathbf{n}$ is the unit normal to $\partial\Omega_f$. The viscous characteristic length Λ and the through-thickness high-frequency tortuosity α_∞ are given by[5,46]

$$\Lambda = 2 \frac{\int_{\Omega_f} \mathbf{E} \cdot \mathbf{E} \, dV}{\int_{\partial\Omega_f} \mathbf{E} \cdot \mathbf{E} \, dS} , \quad \alpha_\infty = \frac{\langle \mathbf{E} \cdot \mathbf{E} \rangle}{\langle \mathbf{E} \rangle \cdot \langle \mathbf{E} \rangle}. \tag{19}$$

Similar to the static viscous permeability and tortuosity parameters introduced in the previous section, these scalar quantities are sufficient to parameterize the homogenized response of the material (owing to macroscopic isotropy).

c. Thermal effects. In the low frequency limit (that is, in the static case), heat diffusion in porous media is governed by the Poisson equation,[42]

$$\nabla^2 \tau = -1, \tag{20}$$

in Ω_f, with $\tau = 0$ on $\partial\Omega_f$ and τ is $\partial\Omega$-periodic. The static thermal permeability k_0' and static thermal tortuosity α_∞ are finally estimated as[40]

$$k_0' = \langle \tau \rangle , \quad \alpha_0' = \frac{\langle \tau^2 \rangle}{\langle \tau \rangle^2}. \tag{21}$$

As an illustration, Fig. 6 shows the solution fields obtained by the finite element method (with a $\mathbb{P}_2 - \mathbb{P}_1$ formulation) for a cubic domain of edge length 2.5 d.

3. Determination of the sound absorption coefficient

Within the framework of the equivalent-fluid theory,[46] the air in a porous medium is replaced by an equivalent fluid that exhibits (i) the same bulk modulus as the saturating air, and (ii) a dynamic density that takes into account the viscous and the inertial interactions with the frame. The determination of these two dynamic parameters subsequently enables the estimation of the wavenumber and characteristic impedance, which in turn can be used to define some relevant properties of the air-filled porous media. In the model,[5,6,9] developed following this macroscopic perspective, the effective density and the effective bulk modulus are respectively defined as

$$\tilde{\rho}(\omega) = \frac{\rho_0 \tilde{\alpha}(\omega)}{\phi} , \quad \tilde{K}(\omega) = \frac{\gamma P_0}{\phi} \frac{1}{\tilde{\beta}(\omega)}, \tag{22}$$

where ρ_0 is the density of the saturating fluid (here, the air), $\gamma = C_p/C_v$ where C_p is the pressure volume-specific heat and C_v is the constant pressure-specific heat, P_0 is the atmospheric pressure, and ϕ is the open porosity. The dynamic tortuosity and dynamic compressibility, denoted by $\tilde{\alpha}(\omega)$ and $\tilde{\beta}(\omega)$ respectively, are then evaluated as

$$\begin{aligned} \tilde{\alpha}(\omega) &= \alpha_\infty \left[1 + \frac{1}{j\varpi'} \tilde{F}(\omega) \right] , \\ \tilde{\beta}(\omega) &= \gamma - (\gamma - 1) \left[1 + \frac{1}{j\varpi'} \tilde{F}'(\omega) \right]^{-1} , \end{aligned} \tag{23}$$

where j is the imaginary unit, $\tilde{F}(\omega)$ and $\tilde{F}'(\omega)$ are the dimensionless viscous and thermal shape functions depending on the dimensionless viscous and thermal angular frequencies (denoted by ϖ and ϖ', respectively), defined as

$$\begin{aligned} \tilde{F}(\omega) &= 1 - P + P \sqrt{1 + \frac{M}{2P^2} j\varpi} , \\ \tilde{F}'(\omega) &= 1 - P' + P' \sqrt{1 + \frac{M'}{2P'^2} j\varpi'} , \end{aligned} \tag{24}$$

with

$$\varpi = \omega \frac{\rho_0 k_0 \alpha_\infty}{\phi \eta} , \quad \varpi' = \omega \frac{k_0' \rho_0 C_p}{\phi \kappa} , \tag{25}$$

where η and κ are the dynamic viscosity and the thermal conductivity of the air, respectively. The four non-dimensional shape factors M, M', P, and P' only depend on the material transport parameters introduced in Sec. III B 2,

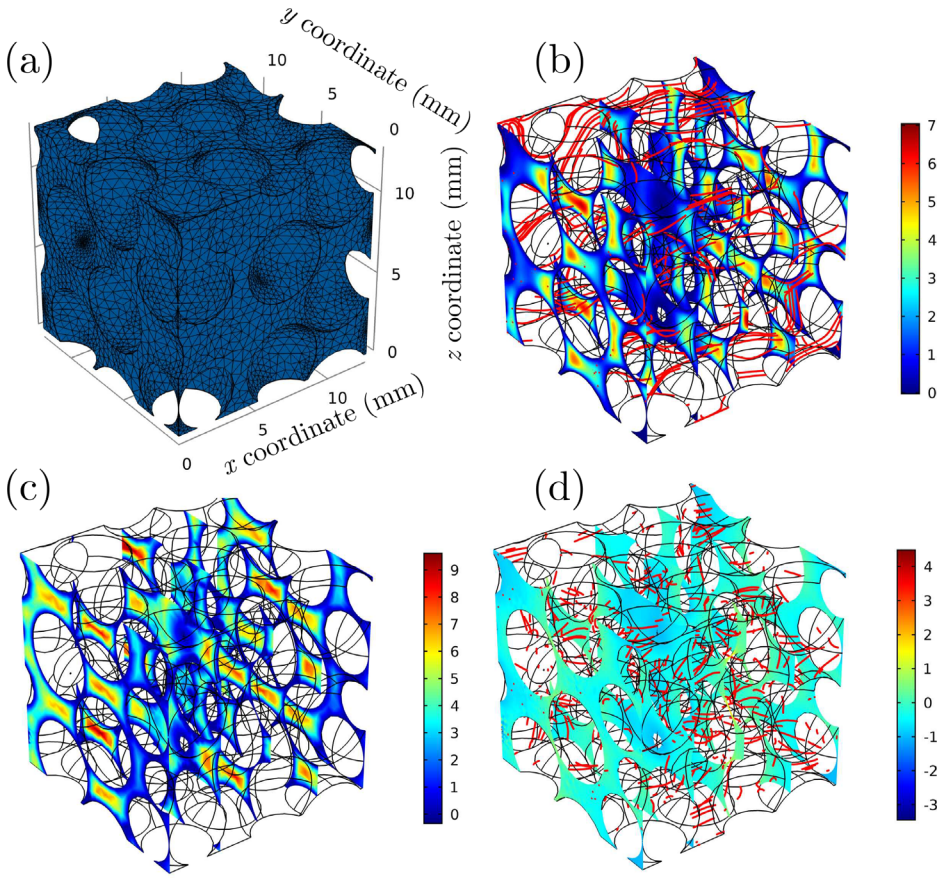

FIG. 6. (Color online) Asymptotic solution fields: (a) mesh containing 58 400 Lagrangian tetrahedral elements; (b) low-frequency scaled velocity field $\mathbf{k}_0^* \cdot \mathbf{e}$ [$\times 10^{-8}$ m^2] obtained for $\mathbf{e} = (1, 0, 0)$; (c) low-frequency scaled temperature field τ [$\times 10^{-8}$ m^2]; (d) high-frequency scaled velocity field $\mathbf{E} \cdot \mathbf{e}$ [$-$] for an external unit field $\mathbf{e} = (1, 0, 0)$.

$$M = \frac{8k_0\alpha_\infty}{\Lambda^2\phi}, \quad P = \frac{M}{4(\alpha_0/\alpha_\infty - 1)},$$
$$M' = \frac{8k_0'}{\Lambda'^2\phi}, \quad P' = \frac{M'}{4(\alpha_0' - 1)}. \tag{26}$$

It should be noticed that the so-called Johnson-Champoux-Allard (JCA) and Johnson-Champoux-Allard-Lafarge (JCAL) models are recovered by letting $M' = P = P' = 1$ and $P = P' = 1$, respectively.

For a homogeneous acoustic layer, the wavenumber $\tilde{k}(\omega)$ and the characteristic impedance $\tilde{Z}_c(\omega)$ can be calculated by

$$\tilde{k}(\omega) = \omega\sqrt{\frac{\tilde{\rho}(\omega)}{\tilde{K}(\omega)}}, \quad \tilde{Z}_c(\omega) = \sqrt{\tilde{\rho}(\omega)\tilde{K}(\omega)}. \tag{27}$$

In the third and final step, the sound absorption coefficient at normal incidence of the absorbing porous layer backed by a rigid wall is defined as

$$\alpha^{\text{sim}}(\omega) = 1 - \left|\frac{\tilde{Z}_s(\omega) - Z_0}{\tilde{Z}_s(\omega) + Z_0}\right|^2, \tag{28}$$

where Z_0 is the characteristic impedance of ambient air and $\tilde{Z}_s(\omega) = -j\tilde{Z}_c(\omega)\cot[\tilde{k}(\omega)L]$ is the surface impedance on the free face of the sample having thickness L.

4. Numerical results

The entire set of transport parameters for the sphere-packing microstructure is reported in Table II for the specific case $d = 5$ mm. These parameters provide information relevant to the propagation and dissipation phenomena in the equivalent homogeneous material, in accordance with the multiscale setting, and allows one to estimate the sound absorption coefficient $\alpha(\omega)$ (following the derivations in the previous sections).

In order to build the mapping $\boldsymbol{\mu} \mapsto \{\alpha^{\text{sim}}(\omega; \boldsymbol{\mu}), \omega \in \mathbb{W}\}$, samples of $\boldsymbol{\mu}$ are drawn from the product of uniform probability measures on the intervals [1, 10] mm (for the diameter d) and [5, 100] mm (for the sample thickness L). Note that these intervals are relevant to a broad range of absorber configurations, as discussed in Ref. 33. Results obtained for the ten configurations defined in Table III are displayed in Fig. 7.

C. Deploying the methodology

For numerical purposes, we consider discretized expansions associated with a frequency step of 4 Hz. Notice that

TABLE II. Transport properties computed for $d = 5$ mm.

ϕ [-]	Λ' [mm]	Λ [mm]	k_0 [$\times 10^{-8}$ m^2]	k_0' [$\times 10^{-8}$ m^2]	α_∞ [-]	α_0 [-]	α_0' [-]
0.37	0.97	0.70	1.75	2.56	1.46	2.29	1.67

https://doi.org/10.1121/10.0010187

TABLE III. List of parameters for the virtual sphere-packing samples analyzed in Fig. 7.

	Sample name									
Parameter	V1	V2	V3	V4	V5	V6	V7	V8	V9	V10
Diameter, d [mm]	5.24	3.07	8.60	2.75	3.03	2.54	3.05	4.92	3.79	9.31
Thickness, L [mm]	93.24	74.38	51.42	59.96	27.54	48.59	96.49	56.95	54.51	27.00

the results reported in this section are displayed in terms of frequency f.

1. Statistical reduction for the computational surrogate

The first step of the methodology consists in analyzing the reduction of the process $\{\alpha^{\text{sim}}(\omega), \omega \in \mathbb{W}\}$, based on a set of samples of $\boldsymbol{\mu}$. To identify the number of realizations that are necessary to achieve convergence for the projection basis, we characterize the convergence of the statistical estimator for the covariance matrix of the discretized process, denoted by $[\tilde{C}]$. The graph of the function $N^{\text{sim}} \mapsto |||[\tilde{C}(N^{\text{sim}})]|||$ is shown in Fig. 8, where N^{sim} denotes the number of realizations used to compute the estimator. It is seen that reasonable convergence is achieved for $N^{\text{sim}} = 200$, which is the number considered in subsequent calculations.

We next determine the truncation order ν in the statistical reduction [see Eq. (5)] by analyzing the convergence of the function $m \mapsto \text{Err}(m)$ defined as

$$\text{Err}(m) = 1 - \frac{\sum_{i=1}^{m} \lambda_i^{\text{sim}}}{\text{tr}([\tilde{C}])}. \tag{29}$$

The graph of the error function is shown in Fig. 9. It is found that the error is less than 1×10^{-2} (respectively 1×10^{-4} and 1×10^{-6}) for $m = 10$ (respectively $m = 21$ and $m = 33$). The graphs of the first five eigenfunctions $\{\omega \mapsto \varphi_i^{\text{sim}}(\omega)\}_{i=1}^{5}$ are displayed in Fig. 10. In what follows, we consider a truncation at order $\nu = 21$, and a quantitative comparison between the reference sound absorption coefficient α^{sim} and the truncated KL representation is provided in Fig. 11, for a specific microstructural sample.

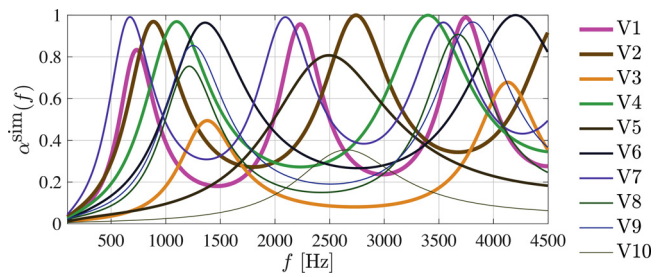

FIG. 7. (Color online) Predicted sound absorption coefficients for the ten virtual samples described in Table III.

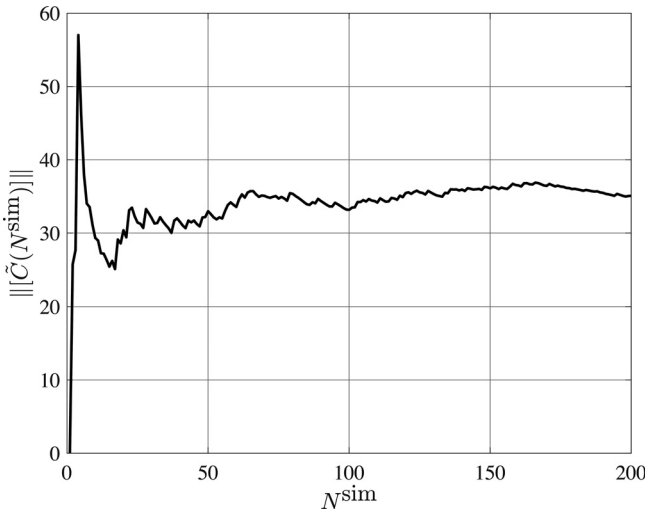

FIG. 8. Graph of the Frobenius norm of the statistical estimator for the covariance matrix, as a function of the number of samples N^{sim}. This figure shows that 200 samples are sufficient to compute $[\tilde{C}]$.

2. Neural network surrogate for the computational reduced coordinates

Following the second step in the approach outlined in Sec. II A, samples for the reduced coordinates associated with the multicale computational model are obtained as

$$\eta_i^{\text{sim}}(\boldsymbol{m}) = \frac{1}{\sqrt{\lambda_i^{\text{sim}}}} \langle \alpha^{\text{sim}}(\bullet\,; \boldsymbol{m}) - \underline{\alpha}^{\text{sim}}, \varphi_i^{\text{sim}} \rangle, \tag{30}$$

where $\boldsymbol{m}$ denotes a realization of $\boldsymbol{\mu}$, and the mapping $\boldsymbol{\mu} \mapsto \boldsymbol{\eta}^{\text{sim}}(\boldsymbol{\mu})$ is approximated by using a neural network (with $\mathcal{I} = 2$ and $\mathcal{O} = 21$, following the notation introduced in Sec. II B 1). As previously indicated, a feed forward Neural Network (NN) is used in this work, and the architecture was determined through a parametric analysis in terms of N_H (number of hidden layers) and the set $\{n_\ell\}_{\ell=1}^{N_H}$ (number of

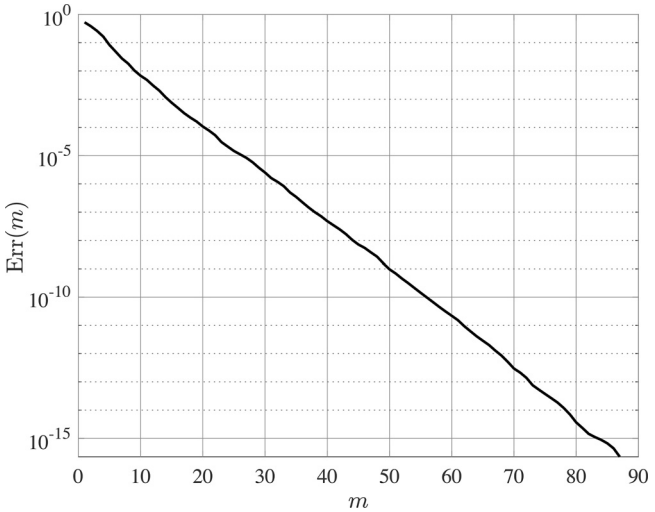

FIG. 9. Graph of the function $m \mapsto \text{Err}(m)$ measuring the error induced by the truncation in the KL decomposition.

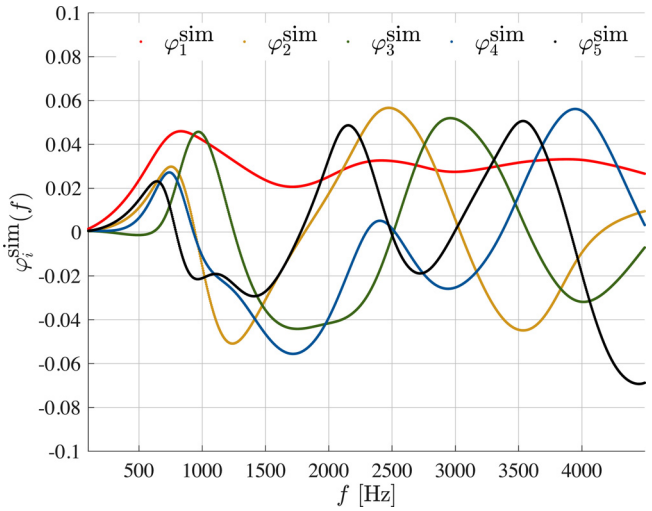

FIG. 10. (Color online) Graph of the five first eigenfunctions which are used to represent the sound absorption coefficient obtained from the multi-scale formulation.

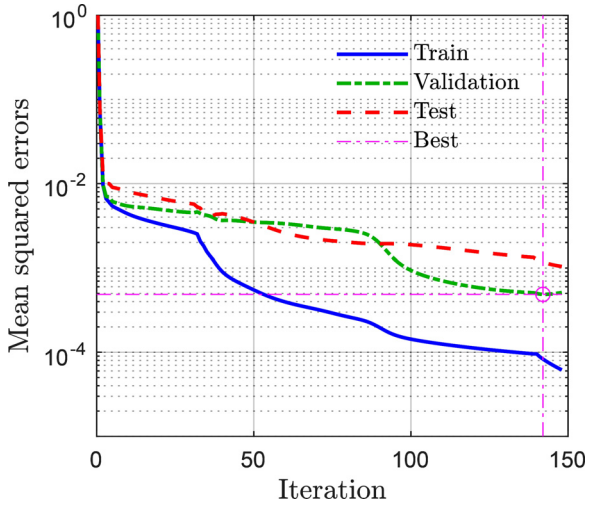

FIG. 12. (Color online) Performance of the proposed NN model within the numerical training dataset: Convergence of the mean squared errors for training, validation, and testing, respectively.

neurons per layer, for all layers). While no attempt was made to fully optimize the architecture for the problem at hand, a structure with five hidden layers and ν, 3ν, ν, ν, and ν neurons per layer, respectively, was found to provide reasonably accurate results (recall that $\nu = 21$). The convergence of the mean squared error for the training, validation, and testing stages can be seen in Fig. 12. Here, the training, validation, and testing sets were composed of 144, 18, and 18 samples, respectively. The prediction obtained by using the NN surrogate with the truncated (KL) expansion for a given sample (not considered during the training process) can be seen in Fig. 13. It is seen that the surrogate predicts the sound absorption response fairly accurately over the whole frequency domain for the virtual sample under consideration. In particular, the location and magnitude of the peaks are well estimated. It should, however, be pointed out that larger (but still contained) discrepancies can be observed on some other samples. The observed errors stem from the combination of the error raised by the truncation in the KL expansion, which can be reduced by increasing ν, and the error generated by the NN surrogate, which may be decreased by refining the architecture and training strategy.

3. Neural network surrogate for the experimental reduced coordinates and experimental sound absorption prediction

In the final step of the methodology, transfer learning is applied to approximate the mapping $\boldsymbol{\mu} \mapsto \hat{\boldsymbol{\eta}}^{\text{exp}}(\boldsymbol{\mu})$ with the limited dataset (composed of only ten samples). To this end, a shallow network is added to the neural network constructed and calibrated in Sec. III C 2, with the aim of

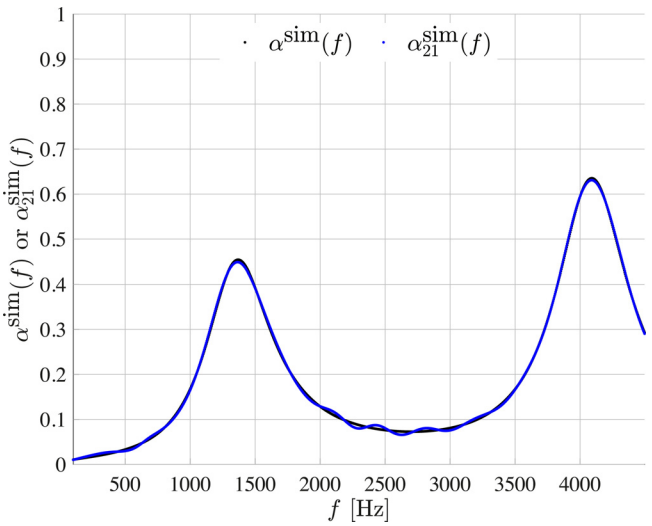

FIG. 11. (Color online) Graphs of the reference function $f \mapsto \alpha^{\text{sim}}(f)$ (black dots) and approximation $f \mapsto \alpha_{21}^{\text{sim}}(f)$ for a truncation order $\nu = 21$ (blue dots) for the virtual sample with $d = 9.61$ mm and $L = 52.00$ mm.

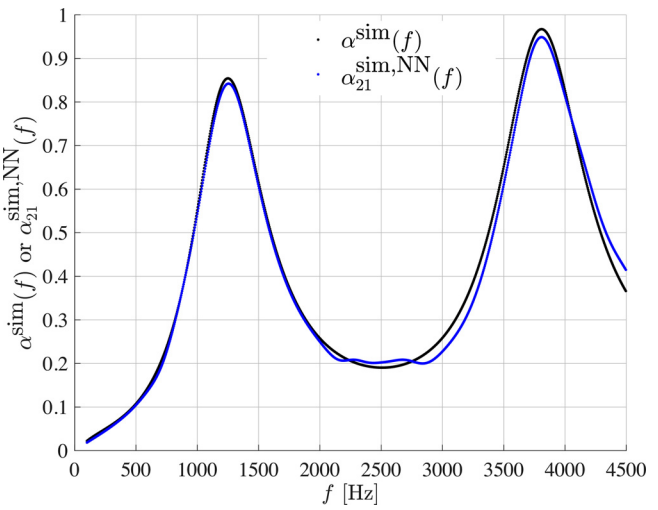

FIG. 13. (Color online) Graphs of the reference function $f \mapsto \alpha^{\text{sim}}(f)$ (black dots) and approximation $f \mapsto \alpha_{21}^{\text{sim,NN}}(f)$ defined through the KL expansion ($\nu = 21$) and the NN model (blue dots) for the virtual sample with $d = 3.8$ mm and $L = 54.51$ mm.

https://doi.org/10.1121/10.0010187

representing the mapping $\boldsymbol{\eta}^{\text{sim}} \mapsto \hat{\boldsymbol{\eta}}^{\text{exp}}$. The additional layer contains ν neurons, and is also optimized with the Levenberg-Marquardt algorithm. Results from the training, validation, and testing stages are reported in Fig. 14. A small number of epochs is necessary to obtain good approximation results in the transfer learning approach, which suggests that the computational surrogate is fairly accurate. The increase in the mean squared error for the validation test suggests overfitting, which may be alleviated through various strategies including model simplification, regularization (with early stopping, for instance), and noise addition to list a few. As stated earlier, no attempt was made to optimize the machine learning part of the framework, given the scope of this study, and refinements along those lines are left for future work.

Finally, the experimental sound absorption coefficient is predicted as

$$\alpha_\nu^{\text{exp,NN}}(\omega) = \underline{\alpha}^{\text{exp}}(\omega) + \sum_{i=1}^{\nu} \sqrt{\lambda_i^{\text{sim}}}\, \hat{\eta}_i^{\text{exp,NN}}\, \varphi_i^{\text{sim}}(\omega), \tag{31}$$

where $\hat{\boldsymbol{\eta}}^{\text{exp,NN}}$ denotes the neural network surrogate calibrated through transfer learning. The graphs of the experimentally-measured sound absorption coefficient α^{exp} and the prediction $\alpha_\nu^{\text{exp,NN}}$ for the physical samples R3 and R7 (see Table I), which were both discarded for training, are shown in Figs. 15 and 16, respectively. It is seen that the hybrid surrogate model combining the KL expansion with the computationally-based projection basis and the neural network calibrated through transfer learning predicts the experimental responses very well, even if only eight experimentally-characterized samples were used as the dataset. While the responses for R3 and R7 remain quite different from one another, the surrogate can properly estimate the locations of small and large peaks, as well as the corresponding magnitudes in both cases. In practice, a normalized L^2 error, defined as

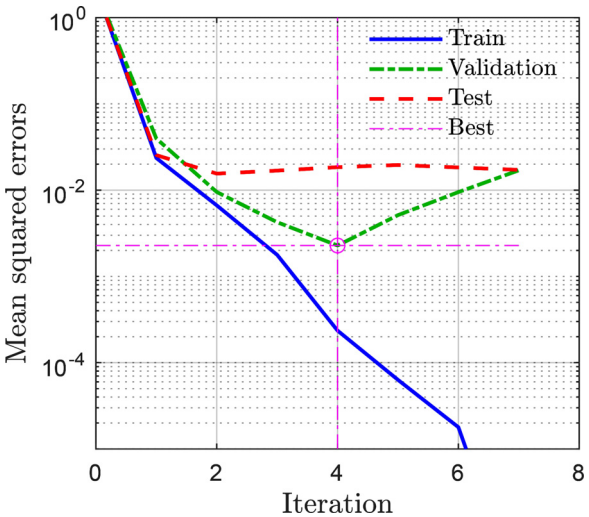

FIG. 14. (Color online) Performance of the proposed NN model within the experimental dataset: Convergence of the mean squared errors for training, validation, and testing, respectively.

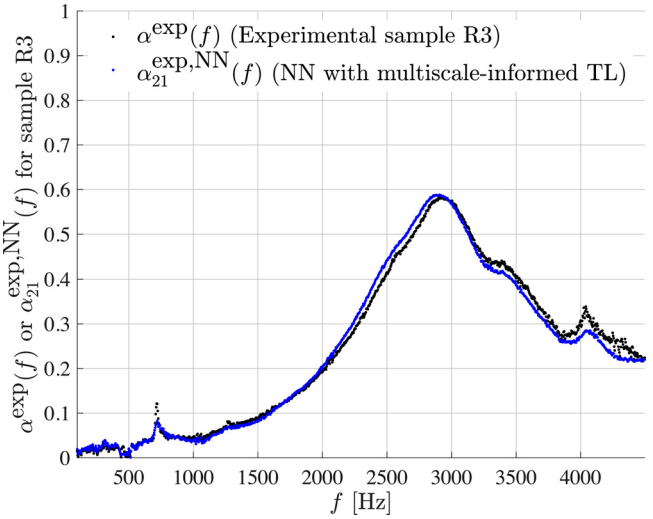

FIG. 15. (Color online) Graphs of the experimentally-measured sound absorption coefficient α^{exp} and neural network prediction $\alpha_{21}^{\text{exp,NN}}$ for sample R3 (see Table I).

$$\varepsilon_\nu = \frac{||\alpha^{\text{exp}} - \alpha_\nu^{\text{exp,NN}}||}{||\alpha^{\text{exp}}||}, \tag{32}$$

can be used to assess the accuracy of the prediction. This error is equal to 5.4% and 5.7% for samples R3 and R7, respectively. Other analyses (which are not reported below for the sake of conciseness) were performed by using other pairs of discarded responses (in lieu of R3 and R7), and similar results were obtained regarding the quality of the approximations. It should be noticed that the asymptotic result $\lim_{\nu\to\infty} \varepsilon_\nu = 0$ holds in the big data limit (which is not the setting considered in this paper), owing to the universal approximation theorem.[47,48] The rate of convergence depends on several factors, among which are the accuracy of the computational model, the architecture of the neural

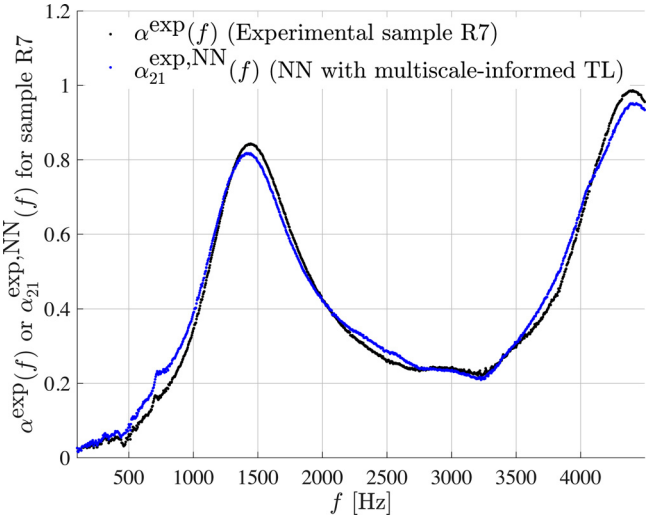

FIG. 16. (Color online) Graphs of the experimentally-measured sound absorption coefficient α^{exp} and neural network prediction $\alpha_{21}^{\text{exp,NN}}$ for sample R7 (see Table I).

TABLE IV. Analytical estimates derived by combining periodic homogenization and the self-consistent scheme. The determination of the characteristic lengths and permeabilities of spherical packings is based on a bicomposite spherical pattern. Here, $R = d/2\beta$ with $\beta = \sqrt[3]{1-\phi}$ (Refs. 43 and 44).

	Method		
Factor	P-estimate	C-estimate	V-estimate
Λ/R	$\frac{2\phi(3-\phi)}{9(1-\phi)}$	$\frac{2\phi(3-\phi)}{9(1-\phi)}$	$\frac{2\phi(3-\phi)}{9(1+\beta^4)(1-\phi)}$
Λ'/R	$\frac{2\phi}{3(1-\phi)}$	$\frac{2\phi}{3(1-\phi)}$	$\frac{2\phi}{3(1-\phi)}$
k_0/R^2	$\frac{2-3\beta+3\beta^5-2\beta^6}{9\beta+6\beta^6}$	$\frac{10-18\beta+10\beta^3-2\beta^6}{45\beta}$	$\frac{4-9\beta+10\beta^3-9\beta^5+4\beta^6}{18(\beta^1-\beta^6)}$
k_0'/R^2	$\frac{3}{2\phi}\frac{10-18\beta+10\beta^3-2\beta^6}{45\beta}$	$\frac{3}{2\phi}\frac{10-18\beta+10\beta^3-2\beta^6}{45\beta}$	$\frac{3}{2\phi}\frac{10-18\beta+10\beta^3-2\beta^6}{45\beta}$

network, and the amount of experimental data available for transfer learning. It is also observed that the sound absorbing spectrum obtained from the recorded time series (Fig. 3) showed some dips and peaks of small amplitudes (at 488, 724, 3324, 3856, and 4056 Hz for sample R5, for instance). Because the pics and dips are not included in the JCAPL rigid-frame analytical model, these additive noise terms suggest a potential influence (related to vibration effects) of the sample holder that is made of a steel wire frame on the sound absorption spectrum (grid size of 2 mm and wire diameter of 0.2 mm) and was not modeled in the simulations. Note that modeling the vibration of the particle frame and casing effects is beyond the scope of the present paper (see, for instance, Ref. 49 and the references therein). Within the context of this study, it is important to note that these small peaks and dips are also captured by the neural network model; see Figs. 15 and 16. Caution must therefore be exercised in using the proposed framework on potentially corrupted data or on data accounting for phenomena that are not included in the model. In the former case, specific techniques based on, e.g., sensitivity analyses and filtering may be deployed to improve robustness at the training stage. In the latter case, additional physical mechanisms may be introduced to enhance the model, depending on the problem of interest.

IV. CONCLUSION

A novel methodology to learn acoustical responses based on limited experimental datasets was presented. From a methodological standpoint, the approach combines a multiscale-informed encoder, used to cast the learning task in a finite-dimensional setting, with a neural network model acting between the set of microstructural descriptors (comprised of the monodisperse particle diameter and the sample thickness in the presented application) and the reduced (latent) variables. The neural network is trained through transfer learning, using synthesized multiscale data to compensate for experimental data scarcity. The relevance of the approach was investigated by considering the prediction of the sound absorption coefficient. It was shown that the proposed strategy allows for the map between the microstructural parameters and the acoustic response to be well approximated, even with limited data.

From an application standpoint, this work demonstrates how the experiments and models typically obtained and developed into several significant contributions to acoustics can be combined to enrich datasets in a context that many researchers in the field of acoustical materials encounter—namely, the identification and validation of models parameterized by micro-/structural features, based on a few experimental samples. The methodology allows one to explore these important aspects with the ability to account for microscopic effects, as well as correlation effects between local properties of the medium. It also paves the way for cost reduction through the efficient exploration of the parameter space for acoustical materials design.

Avenues for future research include refinements on the learning components such as network architecture and

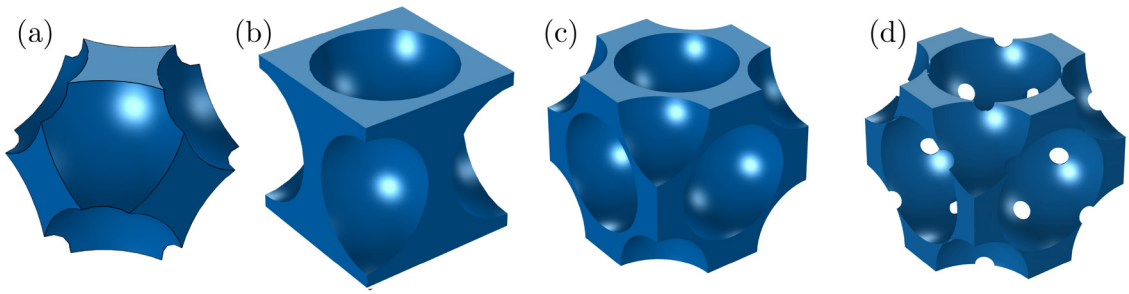

FIG. 17. (Color online) Periodic unit cells of [SC (a), BCC (b), and FCC (c)] at $\phi = 0.42$, and FCC (d) at $\phi = 0.26$ within solder joints with a radius of 150 μm (Ref. 50).

https://doi.org/10.1121/10.0010187

TABLE V. Numerical transport properties for classical lattices of spheres.

Lattice	Reference	Transport parameters							
		ϕ [-]	Λ' [mm]	Λ [mm]	k_0 [$\times 10^{-10}$ m^2]	k_0' [$\times 10^{-10}$ m^2]	α_∞ [-]	α_0 [-]	α_0' [-]
SC	Ref. 51	0.48	0.624	0.369	102	246	1.40	2.02	1.43
	Present		0.621	0.338	103	251	1.38	2.16	1.44
	Ref. 52	0.42	1.56	0.99	535	1457	1.53	2.31	1.45
	Present		1.56	0.99	546	1459	1.53	2.31	1.44
BCC	Ref. 51	0.32	0.325	0.234	19.7	38.1	1.48	2.15	1.35
	Present		0.319	0.189	21.1	37.9	1.47	2.22	1.39
	Ref. 52	0.42	1.43	1.11	435	800	1.32	1.95	1.32
	Present		1.43	1.11	452	803	1.32	1.93	1.31
FCC	Ref. 51	0.26	0.247	0.159	6.70	27	1.65	2.49	1.85
	Present		0.247	0.157	6.76	26.3	1.66	2.65	1.91
	Ref. 52	0.42	1.43	1.12	365	817	1.32	1.86	1.55
	Present		1.42	1.12	393	834	1.32	1.84	1.52

learning strategy, as well as the assessment of the methodology for other acoustical responses (e.g., intrinsic frequency-dependent properties of polydisperse granular structures).

ACKNOWLEDGMENTS

The work of V.-H.T. was supported by the Vietnam National Foundation for Science and Technology Development (NAFOSTED) under Grant No. 107.01-2019.316. The work of J.G. was partially supported by the National Science Foundation, USA, under award DGE-2022040.

APPENDIX A: VALIDATION OF MULTISCALE-INFORMED PREDICTIONS

In this appendix, we report results pertaining to code verification and model validation. Alternative analytical models for transport parameters are first presented in Appendix A 1. Comparisons of multiscale-inferred estimations for the transport properties and the sound absorption coefficient are then proposed in Appendix A 2 and A 3.

1. Analytical models for transport properties

Several analytical models can be used for estimating the transport properties fed as inputs for the JCAPL semi-phenomenological model. Here, we specifically consider three models proposed in Refs. 43 and 44 whose parameters are estimated as follows. The characteristic lengths and permeabilities are defined by the equations listed in Table IV. Three cases are considered, namely, (i) the P-estimate (for which the shear stress vanishes at the boundary); (ii) the V-estimate (for which tangential velocities are equal at the boundary); and (iii) the C-estimate (with vanishing velocity at the boundary). The high-frequency tortuosity factor is defined as $\alpha_\infty = (3-\phi)/2$ for all three cases. The static viscous tortuosities are estimated for $\phi = 0.37$ as $\alpha_{0V} = 1.52$, $\alpha_{0C} = 1.58$, and $\alpha_{0P} = 1.60$. The static thermal tortuosity α_0' is finally equal to 1.94, in agreement with Ref. 33.

2. Validation of the multiscale framework

Three classical cubic lattices are chosen for the sake of verification, namely, simple cubic (SC), body-centered cubic (BCC), and face-centered cubic (FCC) lattices; see Fig. 17. Here, the sphere radius is equal to 1 mm for all patterns. Computational results are compared with those from Refs. 51 and 52 and are found to be in good agreement, see Table V. The evolution of the sound absorption coefficient (at normal incidence) obtained from either the semi-phenomenological models (fed with transport parameters) or the direct numerical approach presented in Ref. 50 is shown

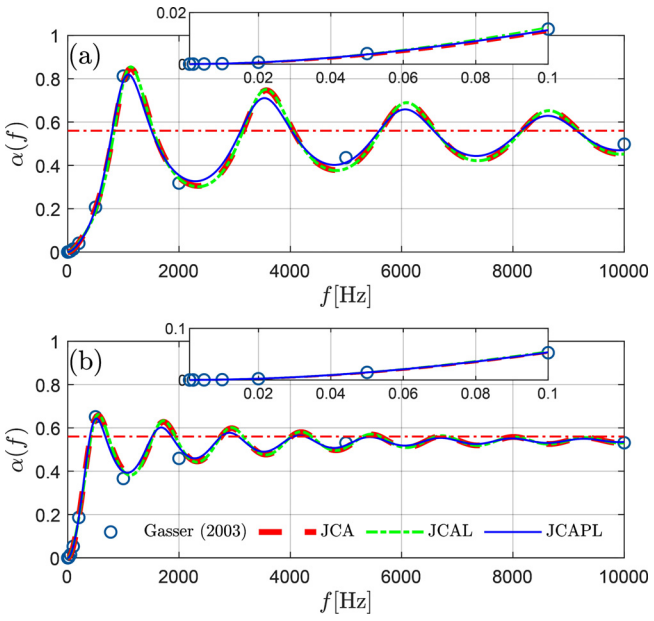

FIG. 18. (Color online) Comparison of the normal incidence sound absorbing behavior obtained with the direct numerical method (circle markers) and a hybrid method based on the JCA model (dashed line), the JCAL model (dash-dotted line), and the JCAPL model (continuous line): (a) $L = 50$ mm and (b) $L = 100$ mm. The inset plots show the same information with a focus on low frequencies (smaller than 0.1 kHz). The horizontal dashed line is the high-frequency sound absorption limit $\alpha_h = 0.56$ for the FCC pattern under study, at a porosity $\phi = 0.26$.

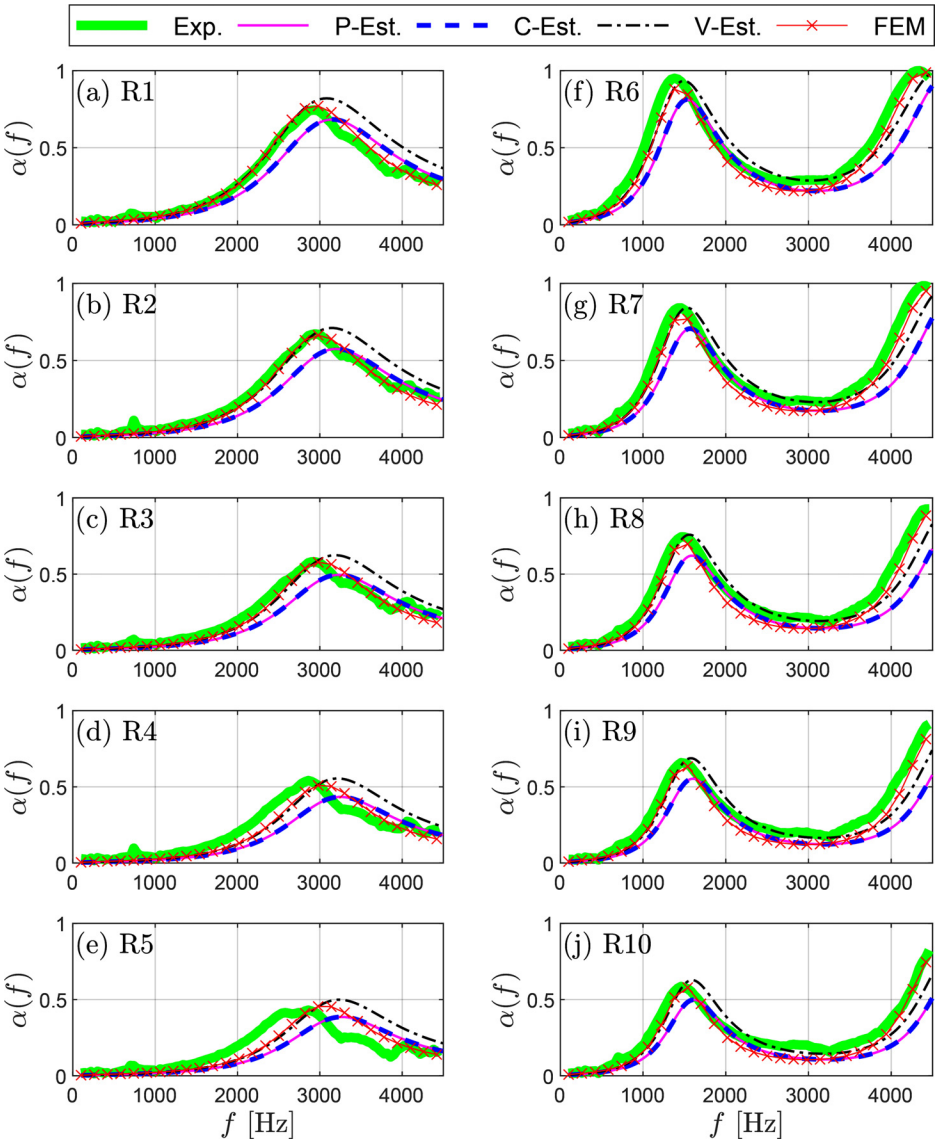

FIG. 19. (Color online) Normal incidence SAC of samples R1 to R5 (left panels a–e) and R6 to R10 (right panels f–j): experiments (green thick continuous line), predictions [P-estimate (magenta continuous line), C-estimate (blue dashed line), and V-estimate (black continuous line)], and FE computations (line with cross-markers).

in Fig. 18. The agreement between the different predictions shows that the hybrid approach allows the sound absorbing behavior to be well described. The absorbers are based on FCC packings [Fig. 17(d)] having two different thicknesses, $L \in \{50, 100\}$ mm. The considered frequencies range between 1 to 10 000 Hz. In the direct approach, the Sound Absorption Coefficient (SAC) value is estimated from the effective factors $\tilde{\rho}(\omega)$ and $\tilde{\beta}(\omega)$ taken from Tables 3.4 and 3.5 in Ref. 50. In agreement with results published elsewhere,[19,33,51] the normal incidence sound absorption coefficient of sphere-packed porous absorbers exhibits quarter-wavelength resonances (see also Sec. III A), and oscillates around the high-frequency sound absorption limit, $\alpha_h = 1 - [(\hat{z}-1)/(\hat{z}+1)]^2$ with $\hat{z} = \phi/\sqrt{\alpha_\infty}$.[53]

3. Comparison of multiscale-informed sound absorption predictions

The predictions of the normal incidence SAC obtained from different approaches are compared below. The experimentally-measured sound absorbing behavior of the ten real samples introduced in Table I is compared with both simulations (combining the JCAPL model with the finite element results on dense random packing of equal spheres) and analytical estimates (combining the JCAPL model with the self-consistent estimates described in Appendix A 1).[43,44] In general, the hybrid multi-scale numerical approach is shown to provide a fairly good estimate of the experimental behavior, as seen in Fig. 19. However, as the particle diameter to sample thickness ratio increases (samples R4 and R5), border effects become significant in the experimental response and a RVE model is less appropriate to simulate such configurations [Figs. 19(d) and 19(e)].

[1]C. Zwikker and C. W. Kosten, *Sound Absorbing Materials* (Elsevier, Amsterdam, 1949).
[2]M. A. Biot, "Theory of propagation of elastic waves in a fluid-saturated porous solid. I. Low-frequency range," J. Acoust. Soc. Am. **28**(2), 168–178 (1956).
[3]M. A. Biot, "Theory of propagation of elastic waves in a fluid-saturated porous solid. II. Higher frequency range," J. Acoust. Soc. Am. **28**(2), 179–191 (1956).
[4]K. Attenborough, "Acoustical characteristics of porous materials," Phys. Rep. **82**(3), 179–227 (1982).

[5]D. L. Johnson, J. Koplik, and R. Dashen, "Theory of dynamic permeability and tortuosity in fluid-saturated porous media," J. Fluid Mech. **176**(1), 379–402 (1987).
[6]Y. Champoux and J. F. Allard, "Dynamic tortuosity and bulk modulus in air-saturated porous media," J. Appl. Phys. **70**(4), 1975–1979 (1991).
[7]D. Lafarge, "Propagation du Son dans les matériaux poreux à structure rigide saturés par un fluide viscothermique: Définition de paramètres géométriques, analogie electromagnétique, temps de relaxation" ("Sound propagation in rigid porous materials saturated with a viscothermal fluid: Geometrical parameters, electromagnetic analogy, relaxation times and universality theory"), Ph.D. thesis, Le Mans Université, Le Mans, France (1993), pp. 1–114.
[8]S. R. Pride, F. D. Morgan, and A. F. Gangi, "Drag forces of porous-medium acoustics," Phys. Rev. B **47**(9), 49644978 (1993).
[9]D. Lafarge, P. Lemarinier, J. F. Allard, and V. Tarnow, "Dynamic compressibility of air in porous structures at audible frequencies," J. Acoust. Soc. Am. **102**(4), 1995–2006 (1997).
[10]K. V. Horoshenkov, A. Hurrell, and J.-P. Groby, "A three-parameter analytical model for the acoustical properties of porous media," J. Acoust. Soc. Am. **145**(4), 2512–2517 (2019).
[11]B. Semeniuk and P. Göransson, "Microstructure based estimation of the dynamic drag impedance of lightweight fibrous materials," J. Acoust. Soc. Am. **141**(3), 1360–1370 (2017).
[12]B. Semeniuk, P. Göransson, and O. Dazel, "Dynamic equations of a transversely isotropic, highly porous, fibrous material including oscillatory heat transfer effects," J. Acoust. Soc. Am. **146**(4), 2540–2551 (2019).
[13]B. Semeniuk, E. Lundberg, and P. Göransson, "Acoustics modelling of open-cell foam materials from microstructure and constitutive properties," J. Acoust. Soc. Am. **149**(3), 2016–2026 (2021).
[14]J. L. Auriault and E. Sánchez-Palencia, "Etude du comportement macroscopique d'un milieu poreux saturé déformable" ("Study of the macroscopic behavior of a deformable saturated porous medium"), J. Mec. **16**(4), 575–603 (1977).
[15]E. Sánchez-Palencia, "Non-homogeneous media and vibration theory," in *Lecture Notes in Physics* (Springer, New York, 1980), Vol. 127.
[16]J. L. Auriault, "Dynamic behaviour of a porous medium saturated by a Newtonian fluid," Int. J. Eng. Sci. **18**(6), 775–785 (1980).
[17]S. Gasser, F. Paun, and Y. Bréchet, "Absorptive properties of rigid porous media: Application to face centered cubic sphere packing," J. Acoust. Soc. Am. **117**(4), 2090–2099 (2005).
[18]J. Allard and N. Atalla, *Propagation of Sound in Porous Media: Modelling Sound Absorbing Materials* (John Wiley & Sons, New York, 2009).
[19]T. G. Zieliński, R. Venegas, C. Perrot, M. Červenka, F. Chevillotte, and K. Attenborough, "Benchmarks for microstructure-based modelling of sound absorbing rigid-frame porous media," J. Sound Vib. **483**, 115441 (2020).
[20]M. Yang and P. Sheng, "Sound absorption structures: From porous media to acoustic metamaterials," Ann. Rev. Mater. Res. **47**, 83–114 (2017).
[21]Z. Laly, R. Panneton, and N. Atalla, "Characterization and development of periodic acoustic metamaterials using a transfer matrix approach," Appl. Acoust. **185**, 108381 (2022).
[22]J. Cuenca, P. Göransson, L. De Ryck, and T. Lähivaara, "Deterministic and statistical methods for the characterisation of poroelastic media from multi-observation sound absorption measurements," Mech. Syst. Signal Process. **163**, 108186 (2022).
[23]M. J. Bianco, P. Gerstoft, J. Traer, E. Ozanich, M. A. Roch, S. Gannot, and C.-A. Deledalle, "Machine learning in acoustics: Theory and applications," J. Acoust. Soc. Am. **146**(5), 3590–3628 (2019).
[24]J. H. Jeon, E. Chemali, S. S. Yang, and Y. J. Kang, "Convolutional neural networks for estimating transport parameters of fibrous materials based on micro-computerized tomography images," J. Acoust. Soc. Am. **149**(4), 2813–2828 (2021).
[25]M. Raissi, P. Perdikaris, and G. E. Karniadakis, "Physics-informed neural networks: A deep learning framework for solving forward and inverse problems involving nonlinear partial differential equations," J. Comput. Phys. **378**, 686–707 (2019).
[26]S. De, J. Britton, M. Reynolds, R. Skinner, K. Jansen, and A. Doostan, "On transfer learning of neural networks using bi-fidelity data for uncertainty propagation," Int. J. Uncertain. Quantif. **10**(6), 543–573 (2020).
[27]K. Bhattacharya, B. Hosseini, N. B. Kovachki, and A. M. Stuart, "Model reduction and neural networks for parametric PDEs," SMAI J. Comput. Math. **7**, 121–157 (2021).
[28]G. J. Lord, C. E. Powell, and T. Shardlow, *An Introduction to Computational Stochastic PDEs*, Cambridge Texts in Applied Mathematics (Cambridge University Press, Cambridge, UK, 2014).
[29]I. Goodfellow, Y. Bengio, and A. Courville, *Deep Learning* (MIT Press, Cambridge, MA, 2016).
[30]S. J. Pan and Q. Yang, "A survey on transfer learning," IEEE Trans. Knowl. Data Eng. **22**(10), 1345–1359 (2010).
[31]K. Weiss, T. M. Khoshgoftaar, and D. Wang, "A survey of transfer learning," J. Big Data **3**(9), 1–40 (2016).
[32]O. Doutres, Y. Salissou, N. Atalla, and R. Panneton, "Evaluation of the acoustic and non-acoustic properties of sound absorbing materials using a three-microphone impedance tube," Appl. Acoust. **71**(6), 506–509 (2010).
[33]V. V. Dung, R. Panneton, and R. Gagné, "Prediction of effective properties and sound absorption of random close packings of monodisperse spherical particles: Multiscale approach," J. Acoust. Soc. Am. **145**(6), 3606–3624 (2019).
[34]V. Voronina and K. Horoshenkov, "Acoustic properties of unconsolidated granular mixes," Appl. Acoust. **65**(7), 673–691 (2004).
[35]H. K. Kim and H. K. Lee, "Acoustic absorption modeling of porous concrete considering the gradation and shape of aggregates and void ratio," J. Sound Vib. **329**(7), 866–879 (2010).
[36]W. S. Jodrey and E. M. Tory, "Computer simulation of isotropic, homogeneous, dense random packing of equal spheres," Powder Technol. **30**(2), 111–118 (1981).
[37]W. S. Jodrey and E. M. Tory, "Computer simulation of close random packing of equal spheres," Phys. Rev. A **32**(4), 2347–2351 (1985).
[38]E. Ghossein and M. Lévesque, "A fully automated numerical tool for a comprehensive validation of homogenization models and its application to spherical particles reinforced composites," Int. J. Solids Struct. **49**(11–12), 1387–1398 (2012).
[39]J. L. Auriault, C. Boutin, and C. Geindreau, *Homogenization of Coupled Phenomena in Heterogenous Media* (John Wiley & Sons, New York, 2010), Vol. 149.
[40]M. Avellaneda and S. Torquato, "Rigorous link between fluid permeability, electrical conductivity, and relaxation times for transport in porous media," Phys. Fluids A **3**(11), 2529–2540 (1991).
[41]Y. Achdou and M. Avellaneda, "Influence of pore roughness and pore-size dispersion in estimating the permeability of a porous medium from electrical measurements," Phys. Fluids A **4**(12), 2651–2673 (1992).
[42]J. Rubinstein and S. Torquato, "Diffusion-controlled reactions: Mathematical formulation, variational principles, and rigorous bounds," J. Chem. Phys. **88**(10), 6372–6380 (1988).
[43]C. Boutin and C. Geindreau, "Estimates and bounds of dynamic permeability of granular media," J. Acoust. Soc. Am. **124**(6), 3576–3593 (2008).
[44]C. Boutin and C. Geindreau, "Periodic homogenization and consistent estimates of transport parameters through sphere and polyhedron packings in the whole porosity range," Phys. Rev. E **82**(3), 036313 (2010).
[45]J. Auriault, "Heterogeneous medium. is an equivalent macroscopic description possible?," Int. J. Eng. Sci **29**(7), 785–795 (1991).
[46]D. Lafarge, "The equivalent fluid model," in *Materials and Acoustics Handbook* (Wiley, Chichester, UK, 2009), pp. 153–204.
[47]G. Cybenko, "Approximation by superpositions of a sigmoidal function," Math. Control Signals Syst. **2**(4), 303–314 (1989).
[48]K. Hornik, M. Stinchcombe, and H. White, "Multilayer feedforward networks are universal approximators," Neural Netw. **2**(5), 359–366 (1989).
[49]T. Tsuruha, Y. Yamada, M. Otani, and Y. Takano, "Effect of casing on sound absorption characteristics of fine spherical granular material," J. Acoust. Soc. Am. **147**(5), 3418–3428 (2020).
[50]S. Gasser, "Etude des proprietes acoustiques et mecaniques d'un materiau metallique poreux modele a base de spheres creuses de nickel" ("Study of acoustical and mechanical properties of a model porous metallic material made of hollow nickel spheres"), Ph.D. thesis, Institut National Polytechnique de Grenoble, Grenoble, France (2003).
[51]C. Y. Lee, M. J. Leamy, and J. H. Nadler, "Acoustic absorption calculation in irreducible porous media: A unified computational approach," J. Acoust. Soc. Am. **126**(4), 1862–1870 (2009).
[52]T. G. Zieliński, "Microstructure-based calculations and experimental results for sound absorbing porous layers of randomly packed rigid spherical beads," J. Appl. Phys. **116**(3), 034905 (2014).
[53]R. Venegas, "Microstructure influence on acoustical properties of multi-scale porous materials," Ph.D. thesis, University of Salford, Salford, UK (2011).